

All-in-fiber multiscan Mach-Zehnder interferometer assisted by core FBG for simultaneous multi-parameter sensing

P. Roldán-Varona^{a,c,*}, D. Pallarés-Aldeiturriaga^{a,b}, L. Rodríguez-Cobo^b, J.M. López-Higuera^{a,b,c}

^aPhotonics Engineering Group, University of Cantabria, 39005, Santander, Spain

^bCIBER-bbn, Instituto de Salud Carlos III, 28029, Madrid, Spain

^cInstituto de Investigación Sanitaria Valdecilla (IDIVAL), 39011, Santander, Spain

Abstract

In this work, a hybrid cladding waveguide (CWG) Mach-Zehnder interferometer (MZI) sensor inscribed by femtosecond laser is demonstrated. The CWG has been inscribed using adaptive optics and multiscan technique. It has been discovered that these waveguides exhibit a phase change dependent of the number of scans performed, allowing free spectral range (FSR) control. Temperature characterization reveals a refractive index change (RIC) proportional and lower than previously reported CWG MZIs, indicating a lower degradation with high temperatures. The CWG proximity to the cladding/air boundary allows good refractive index (RI) sensitivity. Thanks to the FBG inscribed in the reference arm with the point-by-point (PbP) technique, the interferometer can measure curvature and strain simultaneously without being affected by cross-sensitivity.

Keywords: Femtosecond laser, Microstructure fabrication, Optical fiber sensor, Mach-Zehnder, Waveguide.

1. Introduction

The manufacturing of reliable and compact devices in optical fiber exhibits an increased demand due to their intrinsic properties and the possibility of monitoring several parameters simultaneously in a single device [1, 2]. For this purpose, cladding waveguides (CWG) are a key technology to enhance the complexity and possibilities of optical fiber sensors [2]. The manufacture of waveguides as the optical interconnection structure of different sensor elements has enabled the development of more advanced sensor structures, such as optical couplers, waveguide Bragg gratings (WBGs), or interferometers, in their different forms [3, 4]. One of the most straightforward patterns that can be

*Corresponding author

Email address: pablo.roldan@unican.es (P. Roldán-Varona)

manufactured with CWGs is an in-fiber Mach-Zehnder interferometer (MZI). Its main operation principle consists in a CWG decoupling light from core and then coupling it back in order to act as a sensing arm of a MZI instead of using conventional cladding modes. These interferometers are quite versatile, can
 15 measure different parameters and offer the possibility to adjust their sensitivity. They are attractive not only for its enhanced behaviour compared to conventional MZI [5], but also for being a solid step to future next-gen waveguide based devices [6].

This type of interferometers were introduced by several authors independently, measuring different parameters, but not all of them together, as it is
 20 done in this work; thus, proving its intrinsic versatility. Table 1 depicts the sensitivities achieved for each parameter in each work. The temperature has been measured in a low range 25 – 100 °C except in one case [7], achieving sensitivities higher than conventional fiber Bragg gratings (FBGs). Curvature
 25 and strain have been measured in different works independently when these parameters exhibit a high cross-sensitivity. Because of that, they should have been studied simultaneously. In this paper, the joint discrimination of both parameters is undertaken. The refractive index has only been studied once, with great uncertainty.

Table 1. Measured parameters with CWG MZIs in literature.

Ref.	Temperature	Curvature	Strain	RI
[7]	Non linear (50 – 650 °C)	–	–	–
[8]	0.22 nm/°C (20 – 90 °C)	–	4.89 pm/ $\mu\epsilon$	–
[9]	0.6 nm/°C (25 – 100 °C)	–	–	60 nm/RIU ^a
[6]	0.49 nm/°C (50 – 60 °C)	(with FBG)	(with FBG)	(with FBG)
[5]	0.023 nm/°C (25 – 180 °C)	9.49 nm/m ⁻¹	–	–

^a RI Range: 1.33 – 1.34.

In addition of measuring different parameters, the manufacturing of these
 30 devices depends on each application. Thus, it is noteworthy to analyze the different inscription parameters employed in the CWG manufacturing. In Table 2, the reported inscription parameters and types of the waveguides for the previous works are summarized. There is a tendency of employing low-moderate pulse
 35 repetition rate (PRR) (5 – 200 kHz) and pulses/ μm values from 500 to 1200. There are three types of inscriptions depending on the method employed to deal with the wavefront distortion caused by the cylindrical geometry of optical fibers. Waveguides can be inscribed without addressing the distortion, exploiting the filamentation effect [5]. As a solution to induced aberration, they can
 40 also be inscribed with an oil-immersed objective [8, 9], or employing an adaptive optics arrangement [6]. Although it has not been used notably in the literature, in the last two types, the multiscan technique can be used, which will be developed in the next section. Multiscan technique is more relevant since it offers great control of the waveguide properties, such as waveguide diameter and refractive index change (RIC). This versatility encourages further characterization
 45

of its RIC and implications on the transmission spectra of the MZI.

Table 2. Inscription parameters of CWG MZIs in literature.

Ref.	Inscription method	NA	λ (nm)	PRR (kHz)	$\frac{\text{pulses}}{\mu\text{m}}$	τ (fs)	E_p (μJ)
[8]	Oil immersion	$\times 100, 1.25$	800	5	500	35	0.5
[9]	Oil immersion	$\times 60, 1.4$	532	200	1000	250	0.12
[6]	Adaptive optics	$\times 100, 0.42$	517	50	1000	220	0.11
[5]	Filamented waveguide	$\times 100, 0.5$	1030	120	1200	370	1.09

In this work, a 6 mm CWG MZI inscribed by multiscan technique will be manufactured, offering a remarkably more complete characterization than in previous works of literature. The characterization will be focused on phase change with each scan, providing an efficient way to control the free spectral range (FSR). Likewise, as a great novelty, for high temperature the relationship between the degradation of the manufactured waveguide (multiscan technique) and that based on filamentation ([5]) is analytically detailed, in order to justify the benefits of the present inscription method. In addition, the number of parameters that this interferometer can measure requires a way to address the cross-sensitivity. This can be achieved by inscribing an FBG in the reference arm. In this way, a hybrid MZI is demonstrated and employed for simultaneous measurements of strain and bending, which are two parameters that share a strong cross-sensitivity as mentioned early. Additionally, the ability of the manufactured sensor to discriminate the surrounding refractive index (SRI) is also demonstrated.

2. Theory and sensor design

In a simple way, Mach-Zehnder interferometers are based on the optical path difference (OPD) that arises when a beam of light is divided into two optical paths, one of which is taken as a reference, while the other acts as a sensor element. When the MZI is manufactured in an optical fiber, it can be understood that the fundamental mode of the core (reference) is decoupled to a secondary mode that propagates during a distance L in a cladding waveguide (sensing element), until it is coupled again, deriving in an OPD that causes an interference defined by the well-known expression [10],

$$I \approx I_c + I_{wg} + 2\sqrt{I_c I_{wg}} \cos\left(\frac{2\pi\Delta n L}{\lambda} + \phi_0\right), \quad (1)$$

where I_c and I_{wg} represent fundamental (core) and secondary (waveguide) irradiances, respectively, $\Delta n = |n_c - n_{wg}|$ corresponds to the effective mode index difference between both modes, L is the length of the waveguide through which the secondary mode propagates, and ϕ_0 the initial phase.

75 The transmission spectrum has a sinusoidal shape in which local minima (known as interference dips) shifts are used to quantify the measured parameter,

$$\lambda_{dip} = \frac{2\pi \cdot \Delta n \cdot L}{\pi(2m + 1) - \phi_0}. \quad (2)$$

Likewise, the free spectral range can be controlled during the inscription of the waveguide, since it depends on its refractive index. FSR is defined as the spectral distance between two successive transmitted intensity maxima or minima for a given wavelength λ_0 :
80

$$FSR \approx \frac{\lambda_0^2}{\Delta n \cdot L}. \quad (3)$$

The proposed sensor design is depicted in Fig. 1. Secondary mode guidance is achieved by inscribing in a single-mode fiber (SMF) a cladding waveguide whose path length is $L \approx 2 \cdot L_1 + L_2$, where L_1 refers to the S-Bend section that decouples the light from the core towards the straight cladding section L_2 ,
85 separated from the core by a transversal distance d , to be subsequently coupled back to the core under an identical S-Bend. The separation angle of the S-Bend section ($\theta = \arctan(d/L_1)$) is proportional to the waveguide coupling losses.

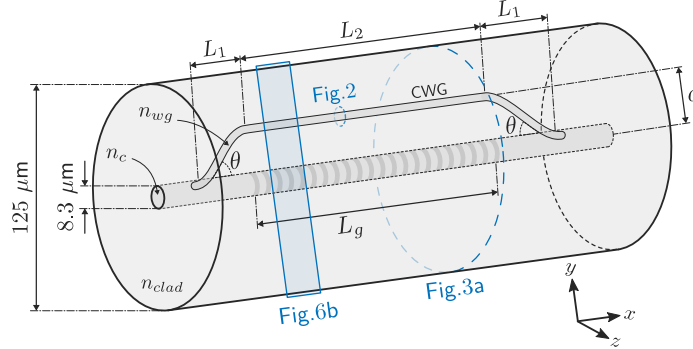


Figure 1. Geometric structure of the all-in-fiber 6 mm component.

Parallel to the MZI cladding section, a FBG of length L_g is inscribed in the
90 core through the point-by-point (PbP) inscription method [2]. The capacity to perform gratings of period $\Lambda \simeq 1 \mu\text{m}$ allows to have a 2nd-order Bragg wavelength in the S-band ($\lambda_B = \frac{2}{m} n_{eff} \Lambda$ with $m = 2$). The grating period is controlled by

$$\Lambda = \frac{v}{PRR}, \quad (4)$$

where v is the writing speed, and PRR is the pulse repetition rate of the laser.

95 2.1. Waveguide inscription: multiscan technique

There are multiple techniques to control the cross-section of femtosecond laser inscribed waveguides. Most of them consist in modifying somehow the conformation of the laser beam, either through active optics [11], spatio-temporal

focusing techniques [12] or slit-beam shaping [13]. However, the multiscan technique is an alternative to these methods: its cross-section is constructed by scanning many times the substrate through the focus of the symmetric rotation laser beam. By combining the lines of modified material induced by each scan it is possible to correct not only the asymmetry of the waveguide, but also its refractive index. This is because the structure of the material depends strongly on its thermal history. The fast cooling suffered by the material after each scan involves an increase in the fictive temperature which, in the case of fused silica (unlike common glass), implies densification [14, 15], and therefore an increase in the refractive index of the waveguide formed by multiple scans. The refractive index change induced in the material is within Type I of permanent modification, that is, a smooth positive isotropic RIC [16].

In Fig. 2, the waveguide manufacture is schematically depicted. It is based on the multiscan technique, through which multiple inscriptions are made, with sub-micron displacements (s) perpendicular to both the laser beam propagation axis and fiber axis between each CWG scan [17]. This “inscribe-and-move” process ends when the structure with the required geometrical properties is obtained, typically when the desired waveguide width (R) is achieved. A series of MZIs was carried out to investigate the values of the parameters that guarantee optimal conditions.

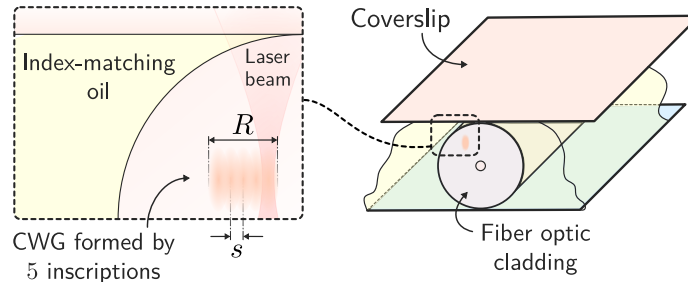


Figure 2. Multiscan technique. Cross-section view of SMF, with multiple inscriptions used in the manufacture of the CWG. Adaptive optics (index-matching oil) is used.

3. Manufacturing

All inscriptions were performed using a commercial femtosecond Fiber Laser Chirp Pulse Amplifier (FLCPA) from CALMAR lasers, operating at 1030 nm, with a 370 fs pulse duration and a variable PRR from 1 Hz to 120 kHz. Laser pulses were focused through an $\times 100$, $NA = 0.5$ objective lens from Mitutoyo. The stripped and stretched optical fiber is located on a slide and covered by a coverslip [18]. As shown in Fig. 2, there is a matching-index oil in the middle that allows to eliminate the cylindrical aberration inherent to the fiber when in-fiber processing is carried out. The slide with the fiber is placed on a platform located on a nanoresolution XYZ motor stage from Aerotech. Using a CCD

camera and a white light source that illuminates the platform, it is possible to
 130 accurately visualize and determine the position of the fiber.

3.1. Cladding waveguide

One of the crucial aspects of the MZI is the light coupling from the core (reference arm) to the CWG (sensing arm). Regarding its design, θ parameter is essential, determined by d and L_1 (Fig. 1). Among the many existing
 135 structures for the coupling of light, two stand out in the existing literature [3]: transition in curve (S-Bend) or transition in straight section. Simulations have been undertaken using Finite Element Beam Propagation Method (FE-BPM), in order to select the most appropriate geometry. The parameters used in the simulation are shown in Table 3. A sweep is performed on L_1 . The schematic
 140 diagrams with the notation used in the simulated structures are depicted in Fig. 3, which also corresponds to the coupling section of Fig. 1.

Table 3. Parameters used in the CWG simulations (FE-BPM)

n_{clad}	1.4661
d	$40 \mu\text{m}$
R	$4 \mu\text{m}$
Δn_{wg}	$5 \cdot 10^{-3}$
Mode	LP_{01}
L_1	$[250, 5000] \mu\text{m}$

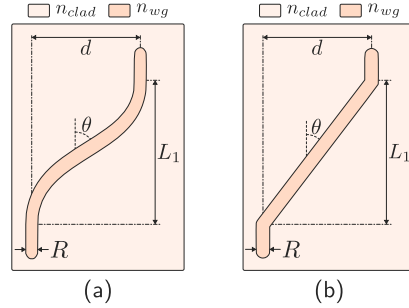


Figure 3. Schematic diagram of the simulated structures, with the parameters indicated in Table 3. (a) S-Bend transition, (b) and straight transition.

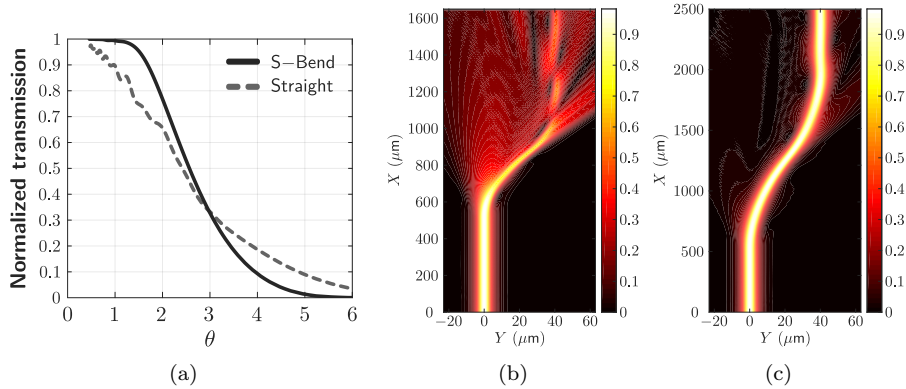


Figure 4. (a) Normalized transmission of LP_{01} mode based on separation angle (θ) for straight and S-Bend transitions. (b) S-Bend example with $L_1 = 650 \mu\text{m}$ ($\theta = 3.52^\circ$). (c) S-Bend example with $L_1 = 1000 \mu\text{m}$ ($\theta = 2.29^\circ$).

Taking into account that, due to physical restrictions, it is interesting to make a compact sensor, values of $L_1 < 1500 \mu\text{m}$ are chosen. In that case S-Bend transitions are more appropriate than straight transitions, limiting losses in the coupling. In Fig. 4, the simulation results are shown.

After modelling and experimental inscriptions, it has been found that the following parameters cause a cladding waveguide with the appropriate symmetry and light guidance. The S-Bend sections have a length $L_1 = 1 \text{ mm}$ (Fig. 4c), while the cladding section has a length $L_2 = 4 \text{ mm}$, identical to the length L_g of the FBG located in the core. The MZI cladding section is transversally separated $d = 40 \mu\text{m}$ from the core, which results in a S-Bend transition angle of $\theta = 2.29^\circ$. This angular value limits the coupling losses of the S-Bend section.

Regarding inscription parameters, cladding waveguides have been manufactured using a pulse energy of $0.19 \mu\text{J}$, a PRR of 60 kHz and $800 \text{ pulses}/\mu\text{m}$ ($v = 75 \mu\text{m/s}$).

In Fig. 5, it is depicted the fiber end-face for a waveguide formed by 5 scans, separated by $s = 0.2 \mu\text{m}$ between them, giving rise to a waveguide structure with a width $R \simeq 4 \mu\text{m}$. By illuminating the distal end of the fiber sample with a white light source, two light spots are observed, corresponding to the core and the CWG (Fig. 5a). It can be seen that the CWG presents a remarkable circular symmetry. Fig. 5b shows the 3D profile of the fiber end-face, with the regions corresponding to the core, the CWG and the filament generated during the laser processing. For this, refracted near field (RNF) profilometry was obtained with *Sira Electro-Optics* optical fiber refractive index profiler.

Fig. 5c is intended to show the RI profile in the core and the CWG, the latter presenting an RI change of $\Delta n_{wg} = 1.51 \cdot 10^{-3}$. If an RI profile is made on the Z axis in the region of the CWG ($Y = d = 40 \mu\text{m}$), it can be distinguished the zones corresponding to the CWG and the filament generated during inscription. Since adaptive optics has been used in the inscription process, the RI change is positive in the focal volume, whereas it is negative in the filamented region ($\Delta n_{fil} = -1.46 \cdot 10^{-3}$). In case of not using adaptive optics, the RI change is negative in the focal volume and positive in the filament [5].

On the other hand, waveguides have also been characterized through the Quantitative Phase Microscopy (QPM) technique. It is a microscopy method that quantifies the phase change that occurs when the light that illuminates the platform passes an optically dense sample as is the optical fiber [19]. It must be noted that the phase change and the RI change are proportional, being related by the well-known relation

$$\Delta(\Delta n) = \frac{\lambda}{2\pi \cdot z} \Delta\phi, \quad (5)$$

where λ is the wavelength of the illumination source (550 nm), and z is the depth of the inscription (region with different RI).

In order to obtain an exhaustive study of inscribed waveguides by multiscan technique, the phase change associated with waveguides formed between 1 and 10 scans has been characterized. QPM has been used with a defocusing of

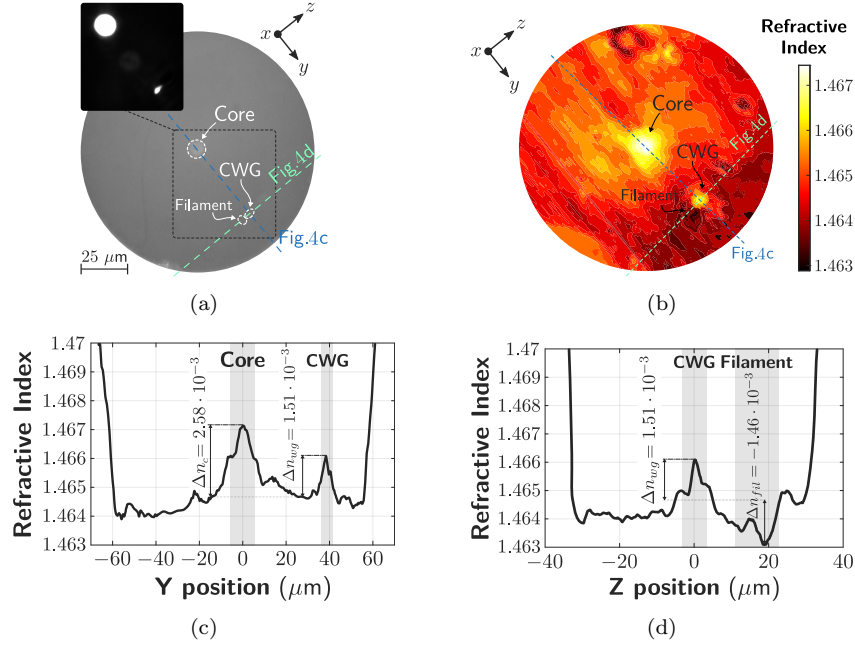


Figure 5. (a) SMF end-face of the waveguide captured with a CCD camera. (b) 3D RI profile measured with a RI Profiler. (c) Core and CWG RI Y profile ($Z = 0 \mu\text{m}$). (d) CWG and filament RI Z profile ($Y = 40 \mu\text{m}$).

185 $\delta z = 3 \mu\text{m}$ and the $\times 100$ objective lens with $\text{NA} = 0.5$. The experimental results of Fig. 6 determine that the lines of modified material induced by each scan cause an increment in the phase change of the waveguide, until reaching a point at which said change tends to stabilize (9 scans). On average, the overlap between consecutive scans is $\sim 72.24\%$. The phase increase is due to the densification caused by the increment in the fictive temperature during multiscan inscription. In a simplified way, two sections with the following slopes can be established:

190

$$m = \frac{\Delta(\Delta\phi)}{\Delta(\#\text{scans})} = \begin{cases} 94.71 \frac{\text{mrad}}{\text{scan}}, & \forall \#\text{scans} \in \mathbb{N} \cap [1, 8]. \\ 0 \frac{\text{rad}}{\text{scan}}, & \forall \#\text{scans} \in \mathbb{N} \cap [9, \infty). \end{cases} \quad (6)$$

The CWG inscription of Fig. 5 was stopped $\sim 10 \mu\text{m}$ before the cleaved end of the fiber, which is why RNF indicates a lower RI change in the CWG than in the core, while QPM indicates a higher phase change in the waveguide than in the core (for 5 scans).

3.2. Mach-Zehnder Interferometer

From now on, waveguides formed by 5 scans will be used to manufacture the MZI, with a refractive index change similar to the core (Fig. 6b), and with a

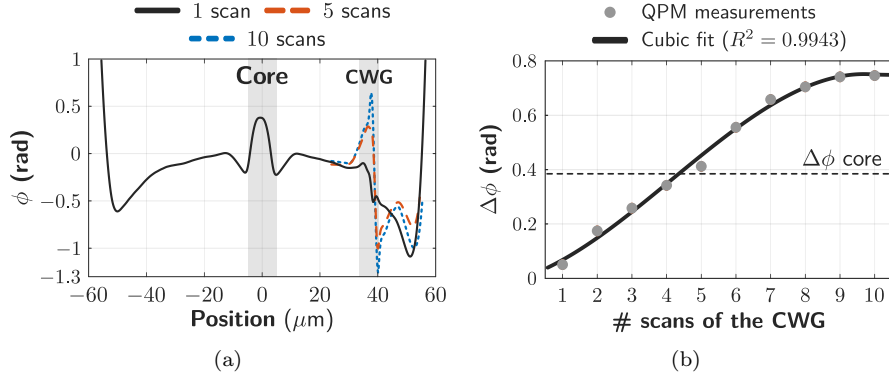


Figure 6. (a) Phase profile measured with QPM for waveguides formed by 1, 5 and 10 scans, (b) and the CWG-cladding phase change based on the number of scans that form the waveguide.

200 circular symmetry that favors light guidance. A greater number of scans would result in structures with an almost rectangular RI profile, hindering the light coupling.

The MZI has been characterized during multiscan inscription. A broadband light source (HP 83437A), and an Optical Spectrum Analyzer (Anritsu MS9740A) have been used in a transmission configuration.

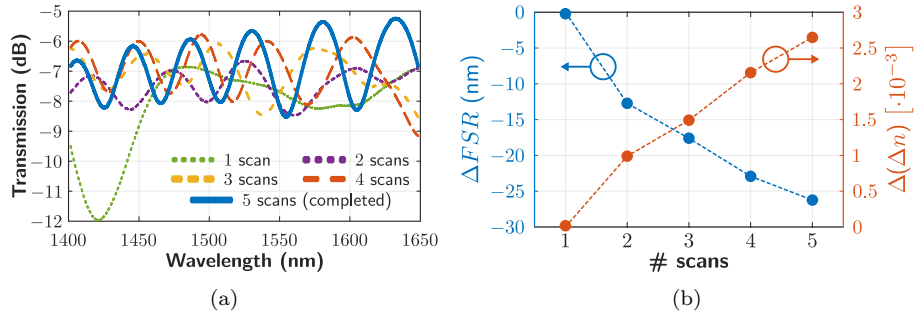


Figure 7. (a) MZI transmission spectra for waveguides formed between 1 and 5 scans. (b) FSR and increment in the effective RI difference depending on the number of scans that make up the CWG (1 – 5 scans). The region 1400 – 1550 nm is selected for the determination of the FSR.

Fig. 7a shows the MZI transmission spectra when the secondary path is formed between 1 and 5 scans. It is noteworthy that the losses caused by the inscription of the sensor are relatively low, standing at approximately 6 dB. Likewise, Fig. 7b shows the variation of the FSR with the number of waveguide scans. FSR values have been extracted from Fig. 7a from the spectral distance between two successive transmitted intensity maximum or minimum. Emphasis is placed on the idea that the multiscan technique is a potential way to control

the properties of an MZI, especially the light coupling and the FSR. According to the relationship shown in Equation 3, reducing the FSR has an associated increase in Δn . From this equation, taking $L \simeq 2L_1 + L_2 = 6$ mm and $\lambda_0 = 1500$ nm, the incremental values of Δn are obtained (Fig. 7b). For a CWG formed by 5 scans, a $\Delta(\Delta n)$ close to $3 \cdot 10^{-3}$ is obtained (taking 1 scan as reference), which approximates the RI change associated with the core, thus validating the results obtained with QPM (Fig. 6b).

3.3. Mach-Zehnder with FBG

The next step is to inscribe the FBG in the core using the PbP method. The manufactured FBG is associated with Type II (damage) grating [20]. The laser is configured with a pulse energy of $0.47 \mu\text{J}$ and a PRR of 10 Hz. The grating period is $\Lambda = 1.051 \mu\text{m}$, which results in a writing speed $v = 10.51 \mu\text{m/s}$ according to Equation 4. Its length is $L_g = 4$ mm, being located parallel to the MZI cladding section. A 2nd-order Bragg wavelength of $\lambda_B = 1516.9$ nm is generated, as it is depicted in Fig. 8a. The Full Width at Half Maximum (FWHM) is ~ 1.19 nm.

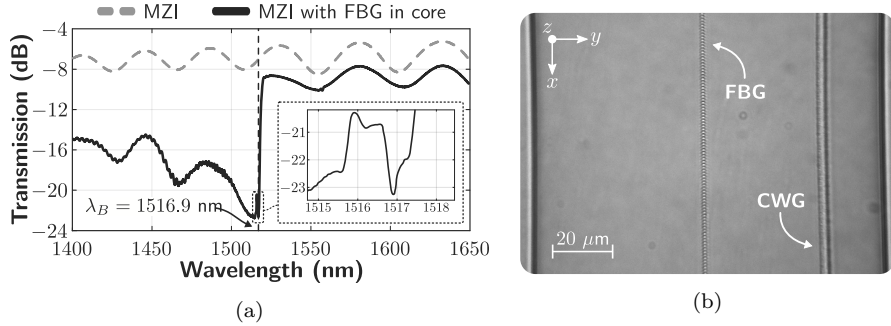


Figure 8. (a) Transmission spectra of the complete MZI (5 scans) without and with the FBG inscription in the core. Inset: zoom of Bragg resonance. (b) Longitudinal view of the MZI cladding section together with the FBG inscription in the core.

4. Experimental results and discussion

First, a temperature analysis will be carried out in order to perform an even more complete characterization of the behavior of the waveguide. In order to achieve this, a comparison is made with the MZI developed by Pallarés-Aldeiturriaga *et al.* [7]. The MZI mentioned presents a filamentary propagation and a birefringent RIC (Type II $\rightarrow \Delta n_{wg} < 0$) as a type of permanent modification in the material [16], with a secondary optical path length $L = 300 \mu\text{m}$. In both cases, an identical temperature cycle has been carried out: it is climbed in steps of 50°C to 800°C , remaining stable for 10 minutes in each step. It should be noted that the Type II MZI is only evaluated up to 650°C , the temperature at which the structure is erased. A notable difference is that, in this paper,

240 a pre-annealing has been carried out by placing the device 6 hours at 200°C. The purpose is to improve the repeatability of the sensor in a medium-high temperature range, as well as to eliminate laser-induced stress changes from the structure.

245 The experimental results, together with those collected from the study carried out in [7], are shown in Fig. 9. It is depicted the shift of the interference dips ($\Delta\lambda_{dip}$) of both MZIs, and the Bragg wavelength shift ($\Delta\lambda_{Bragg}$) corresponding to the FBG. The process of annealing is appreciated in the temperature steps, in which, remaining the temperature stable for 10 min, a shift of λ_{dip} occurs. This is a consequence of the stress relaxation that takes place in the waveguide. As the stress can cause anisotropic and inhomogeneous distribution of the refractive index in the waveguide, the annealing process originates a better behavior of the MZI, since the refractive index is smoothed. Although annealing occurs in both MZIs, the phenomenon is more pronounced in the one manufactured in this work, as it presents a significantly higher sensitivity.

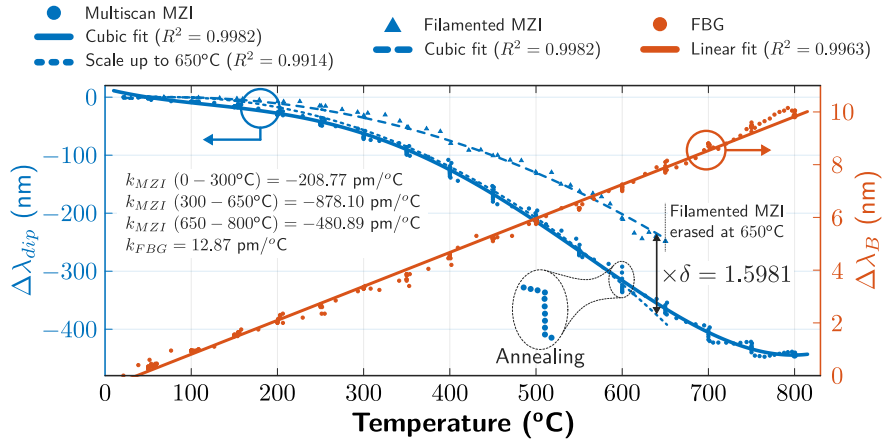


Figure 9. (Left Y axis) Wavelength shift of a interference dip of the MZI developed in this work for temperatures between 23°C and 800°C (continuous line), and wavelength shift of a interference dip of the MZI developed in [7] for temperatures between 23°C and 650°C, with fit and translation (scale factor α) to the measurements of the present work (dotted lines). (Right Y axis) Bragg wavelength shift for temperatures between 23°C and 800°C. The sensitivities (k_T) as well as the effect of the annealing are indicated.

255 The cubic fit of the filamented MZI measurements presents a remarkable coincidence ($R^2 = 0.9914$) with the cubic fit of the multiscan MZI measurements when applying a scale factor $\delta = 1.5981$. This fact has a very important implication, which is developed below.

260 In order to establish a common starting point between the two MZIs, it is considered $(\lambda_{dip})_1(T) = (\lambda_{dip})_2(T)$ at a temperature T , referring 1 to multiscan

MZI and 2 to filamented MZI. According to Equation 2:

$$(\Delta n_{wg})_1(T) \cdot \gamma_1 = (\Delta n_{wg})_2(T) \cdot \gamma_2, \quad (7)$$

$$L_i(T) \approx L_i$$

$$\text{with } \gamma_i \approx \frac{2\pi L_i}{\pi(2m_i + 1) - \phi_i}, \quad \text{being } L_i = \begin{cases} 6 \text{ mm}, & i = 1 \\ 300 \text{ } \mu\text{m}, & i = 2 \end{cases}$$

Defining $(\Delta \lambda_{dip})_i(T)$ as

$$(\Delta \lambda_{dip})_i(T) = (\lambda_{dip})_i(T) - (\lambda_{dip})_i(23^\circ\text{C}) = f_i(T), \quad (8)$$

$$\begin{cases} f_1(T) = \delta \cdot f_2(T) \rightarrow \text{Cubic fit multiscan MZI} \\ f_2(T) \rightarrow \text{Cubic fit filamented MZI} \end{cases} \quad (9)$$

Taking increments on Equation 2, and applying the equality of Equation 8

$$(\Delta \lambda_{dip})_i(T) = [\Delta (\Delta n_{wg})]_i(T) \cdot \gamma_i = f_i(T). \quad (10)$$

265 Finally, according to the relationship indicated in (9), the following equality is obtained

$$\boxed{[\Delta (\Delta n_{wg})]_1(T) = \gamma \cdot [\Delta (\Delta n_{wg})]_2(T), \quad \gamma = \delta \frac{\gamma_2}{\gamma_1}.} \quad (11)$$

270 Thus, it is demonstrated that the variation of the RI with the temperature, for the waveguides of both MZI (filamented Type II, and multiscan Type I), are related through a constant of proportionality γ . From the data obtained with the RNF Profiler, simulations have been applied by means of the Finite Element Method (FEM) in order to obtain the effective mode index difference. In this way, it is possible to estimate γ from Equation 7, taking $T = 23^\circ\text{C}$, temperature at which the RI measurements of the waveguides have been made.

275 The obtained result is coherent insofar as the MZI based on the filamentary propagation presents a RI change higher than the MZI made by multiscan technique, so it has a degradation $\gamma^{-1} = 2.6129$ higher. Hence, at 650°C the filamented MZI is erased, while the MZI developed in this work is still maintained at 800°C .

4.1. Refractive Index

280 The $40 \text{ } \mu\text{m}$ separation of the CWG (multiscan technique) from the core causes a high sensitivity of the MZI to the surrounding RI. Due to this, the MZI was immersed in six different liquids with variations in its refractive index of the order of 10^{-3} . Specifically, these are solutions with sugar concentrations (solute) of 0, 20, 40, 60, 80 and 100 grams per 100 of water (solvent). The refractive index of each liquid has been measured with the Krüss Optronic DR-285 6100 refractometer. The measurement process has been carried out by fixing the fiber and surrounding it with the different liquids.

In Fig. 10 the wavelength shift of the MZI interference dips is observed for the six liquids. Air has been taken as the reference point ($RI = 1 \rightarrow \Delta\lambda_{dip} = 0$).
 290 The developed MZI has a sensitivity of $k_{RI} = 86.52$ nm/RIU (Refractive Index Unit) (higher than [9] at that RI range), being able to detect minimal variations of the medium surrounding the fiber.

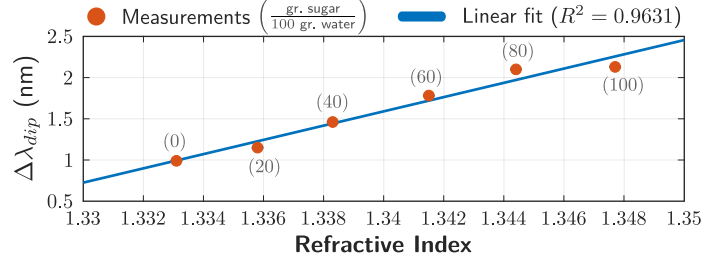


Figure 10. Wavelength shift of a MZI interference dip when immersing the fiber in liquids of different refractive index.

The operational principle behind the behavior is easily justifiable from Equation 2, since it is the variation of λ_{dip} that is monitored during the measurement.
 295 By placing the waveguide near the outside of the fiber, if it is immersed in a liquid with a refractive index higher than that of the air, the effective RI of the waveguide (Δn_{wg}) is increased, causing an increase in λ_{dip} , and in turn, a decrease of the free spectral range.

4.2. Cross-sensitivity

300 Finally, after having sensed temperature and refractive index, the cross-sensitivity of two different parameters is studied. In order to exploit the advantages that the MZI and the FBG provide jointly, joint discrimination of strain (ϵ) and curvature (κ) is proposed. Knowing the variations of both parameters and having their sensitivities, the Bragg and dip wavelength shifts are given by:

$$305 \begin{bmatrix} \Delta\lambda_B \\ \Delta\lambda_{dip} \end{bmatrix} = \begin{bmatrix} k_{\kappa_B} & k_{\epsilon_B} \\ k_{\kappa_{dip}} & k_{\epsilon_{dip}} \end{bmatrix} \begin{bmatrix} \Delta\kappa \\ \Delta\epsilon \end{bmatrix}, \quad (12)$$

being k_{κ} and k_{ϵ} the curvature and strain sensitivities, both being specified for the FBG (k_{-B}) and the MZI (k_{-dip}).

With respect to the curvature, two measurement sets have been made, as it is depicted in Fig. 11a. To perform the measurements, the fiber is clamped on
 310 two platforms separated an initial distance $L_f = 15.2$ cm, being the sensor at the midpoint. One platform remains fixed while the other moves on the X axis. The bending direction must be produced on the Y axis, since the sensitivity obtained is maximum (see Fig. 11a). An estimate of the curvature is achieved through the circumference relation [21]:

$$L_f - x = L_f \cdot \text{sinc} \left(\frac{L_f \cdot \kappa}{2} \right), \quad (13)$$

315 where x refers to the shift of the movable platform on the X axis, and $\kappa = \frac{1}{R}$ is the curvature, the inverse of bending radius R towards bending axis. The sensitivities obtained are $k_{\kappa_B} = -0.0914 \text{ nm/m}^{-1}$ and $k_{\kappa_{dip}} = -30.2578 \text{ nm/m}^{-1}$. The variation of $k_{\kappa_{dip}}$ between both measurement sets is 2.4%.

320 To carry out strain measurements, a fiber section of 15.2 cm length is fixed at its ends, with the sensor in the middle. Subsequently, the fiber is fixed from one point and strained from the other. It is stretched in steps of 0.03 mm to reach 0.63 mm, which results in a maximum strain of $\sim 4150 \mu\epsilon$. According to the results shown in Fig. 11b, the sensitivity obtained for the FBG and the MZI is $k_{\epsilon_B} = 0.7683 \text{ pm}/\mu\epsilon$ and $k_{\epsilon_{dip}} = 0.9839 \text{ pm}/\mu\epsilon$, respectively.

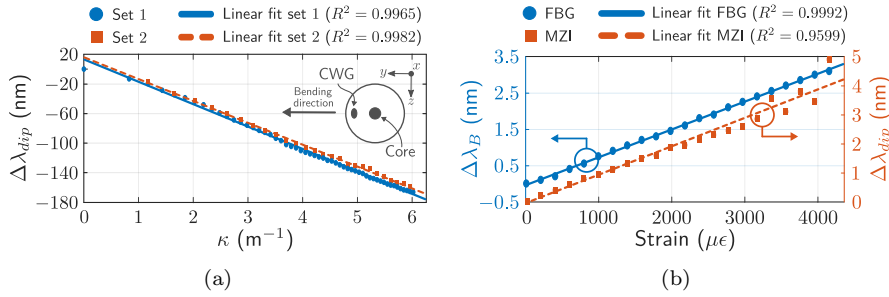


Figure 11. (a) Dip wavelength shift when a curvature sweep is performed. Two sets of measurements are made. (b) Bragg and dip wavelength shift when a strain sweep is applied.

325 At this point, from Equation 12, both measurands can be obtained from the Bragg and dip wavelengths by calculating the inverse matrix of the relation, obtaining the next equality:

$$\begin{bmatrix} \Delta\kappa \\ \Delta\epsilon \end{bmatrix} = \frac{1}{D} \begin{bmatrix} k_{\epsilon_{dip}} & -k_{\epsilon_B} \\ -k_{\kappa_{dip}} & k_{\kappa_B} \end{bmatrix} \begin{bmatrix} \Delta\lambda_B \\ \Delta\lambda_{dip} \end{bmatrix}, \quad (14)$$

where $D = k_{\kappa_B} k_{\epsilon_{dip}} - k_{\kappa_{dip}} k_{\epsilon_B}$ is the matrix determinant.

330 In Fig. 12, the cross-sensitivity of strain and curvature is depicted. It has been obtained by varying a measurand while the other is fixed. For this, the experimental data of Fig. 11 has been used. The applied sweeps show no curvature ($\kappa = 0$) or strain ($\epsilon = 0$), and are depicted (black dotted lines) against the values estimated from the experimental data after applying Equation 14 (dots). Likewise, a linear fit is indicated (color lines) in order to evaluate the error committed. 335 When κ sweep is applied (blue), there is an error of $\sim 7.8\%$ between the real and estimated κ value from the experimental data. Also, the estimated strain (should be null) varies with the curvature according to $-13.4 \mu\epsilon/\text{m}^{-1}$. On the other hand, when strain sweep is applied (orange), the error between the real and estimate strain is $\sim 1.1\%$. In this case, the estimated curvature varies with the strain according to $0.00476 \text{ m}^{-1}/\mu\epsilon$. 340

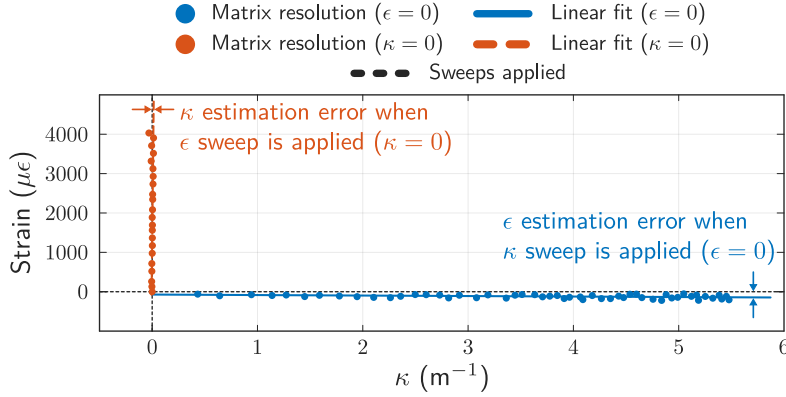


Figure 12. Cross sensitivity of curvature and strain. The graph is obtained by varying one measurand while the other is fixed.

5. Conclusion

In this work a hybrid CWG MZI with a FBG inscribed both by a femtosecond laser has been demonstrated. The CWG has been inscribed employing the multiscan technique that allows control of both width and RIC, as the latter increases with the increment of fictive temperature produced by each scan. In this way, the number of scans is a way to control FSR of the MZI. The temperature characterization of the multiscan waveguide reveals a shift (compared to the filamented waveguide) attributed to a decrement of RIC of the CWG caused by annealing. This change ratio has been proven to be proportional to the one exhibited by filament waveguides, being the latter more degraded with temperature. In addition, given the proximity of CWG to the cladding/air boundary, the interferometer exhibits higher sensitivity to RI than previously reported MZIs at 1.33 – 1.35 range. The FBG inscribed at the reference arm has been employed to independently measure both curvature and strain with cross-sensitivities as low as $-13.4 \mu\epsilon/m^{-1}$ and $0.00476 m^{-1}/m\epsilon$.

Funding

This work has been supported by the project TEC2016-76021-C2-2-R (AEI/FEDER) of the Spanish government and FEDER funds, and by the FPU2018/02797 PhD grant from the Ministry of Science, Innovation and Universities of the Spanish government.

Acknowledgments

The authors would like to thank Matthieu Lancry and Bertrand Pommellec for teaching the QPM method.

References

- 365 [1] Moez Haque, Chemical-Assisted Femtosecond Laser Writing of Lab-in-Fiber Sensors, Ph.D. thesis, University of Toronto (2014).
- [2] C. Waltermann, A. Doering, M. Köhring, M. Angelmahr, W. Schade, Cladding waveguide gratings in standard single-mode fiber for 3D shape sensing, *Optics Letters* 40 (13) (2015) 3109–3112. doi:10.1364/OL.40.003109.
370 URL <https://www.osapublishing.org/abstract.cfm?URI=ol-40-13-3109>
- [3] J. R. Grenier, M. Haque, L. A. Fernandes, K. K. C. Lee, P. R. Herman, Femtosecond Laser Inscription of Photonic and Optofluidic Devices in Fiber Cladding, in: *Planar Waveguides and other Confined Geometries*, Springer New York, 2014, pp. 67–110. doi:10.1007/978-1-4939-1179-0_4.
375
- [4] L. Shah, A. Y. Arai, S. M. Eaton, P. R. Herman, Waveguide writing in fused silica with a femtosecond fiber laser at 522 nm and 1 MHz repetition rate, *Optics Express* 13 (6) (2005) 1999–2006. doi:10.1364/opex.13.001999.
- 380 [5] D. Pallares-Aldeiturriaga, L. Rodriguez-Cobo, A. Quintela, J. M. Lopez-Higuera, Curvature Sensor Based on In-Fiber Mach-Zehnder Interferometer Inscribed with Femtosecond Laser, *Journal of Lightwave Technology* 35 (21) (2017) 4624–4628. doi:10.1109/JLT.2017.2756103.
- [6] A. Theodosiou, A. Ioannou, K. Kalli, All-in-Fiber Cladding Interferometric and Bragg Grating Components Made via Plane-by-Plane Femtosecond Laser Inscription, *Journal of Lightwave Technology* 37 (18) (2019) 4864–4871. doi:10.1109/jlt.2019.2925263.
385
- [7] D. Pallarés-Aldeiturriaga, L. Rodriguez-Cobo, A. Quintela, J. M. Lopez-Higuera, In-fiber Mach-Zehnder interferometer inscribed with femtosecond laser for high temperature sensing, in: Y. Chung, W. Jin, B. Lee, J. Canning, K. Nakamura, L. Yuan (Eds.), *25th International Conference on Optical Fiber Sensors*, SPIE, 2017. doi:10.1117/12.2264991.
390
- [8] W. W. Li, W. P. Chen, D. N. Wang, Z. K. Wang, B. Xu, Fiber inline Mach-Zehnder interferometer based on femtosecond laser inscribed waveguides, *Optics Letters* 42 (21) (2017) 4438–4441. doi:10.1364/OL.42.004438.
395 URL <https://www.osapublishing.org/abstract.cfm?URI=ol-42-21-4438>
- [9] Y. Zhang, C. Lin, C. Liao, K. Yang, Z. Li, Y. Wang, Femtosecond laser-inscribed fiber interface Mach-Zehnder interferometer for temperature-insensitive refractive index measurement, *Optics Letters* 43 (18) (2018) 4421–4424. doi:10.1364/ol.43.004421.
400

- [10] P. Chen, X. Shu, K. Sugden, Ultra-compact all-in-fiber-core Mach-Zehnder interferometer, *Optics Letters* 42 (20) (2017) 4059–4062. doi:10.1364/ol.42.004059.
- [11] A. R. de la Cruz, A. Ferrer, W. Gawelda, D. Puerto, M. G. Sosa, J. Siegel, J. Solis, Independent control of beam astigmatism and ellipticity using a SLM for fs-laser waveguide writing, *Optics Express* 17 (23) (2009) 20853–20859. doi:10.1364/oe.17.020853.
- [12] D. N. Vitek, E. Block, Y. Bellouard, D. E. Adams, S. Backus, D. Kleinfeld, C. G. Durfee, J. A. Squier, Spatio-temporally focused femtosecond laser pulses for nonreciprocal writing in optically transparent materials, *Optics Express* 18 (24) (2010) 24673–24678. doi:10.1364/oe.18.024673.
- [13] M. Ams, G. D. Marshall, D. J. Spence, M. J. Withford, Slit beam shaping method for femtosecond laser direct-write fabrication of symmetric waveguides in bulk glasses, *Optics Express* 13 (15) (2005) 5676–5681. doi:10.1364/opex.13.005676.
- [14] R. Brückner, Properties and structure of vitreous silica. I, *Journal of Non-Crystalline Solids* 5 (2) (1970) 123–175. doi:10.1016/0022-3093(70)90190-0.
- [15] J. W. Chan, T. R. Huser, S. H. Risbud, J. S. Hayden, D. M. Krol, Waveguide fabrication in phosphate glasses using femtosecond laser pulses, *Applied Physics Letters* 82 (15) (2003) 2371–2373. doi:10.1063/1.1565708.
- [16] R. Osellame, G. Cerullo, R. Ramponi (Eds.), *Femtosecond Laser Micromachining*, Springer Berlin Heidelberg, 2012. doi:10.1007/978-3-642-23366-1.
- [17] P. Roldán-Varona, D. Pallarés-Aldeiturriaga, L. Rodríguez-Cobo, J. M. López-Higuera, Hybrid Mach-Zehnder interferometer manufactured by femtosecond laser multiscan technique, in: K. Kalli, G. Brambilla, S. O. O’Keeffe (Eds.), *Seventh European Workshop on Optical Fibre Sensors*, SPIE, 2019. doi:10.1117/12.2538813.
- [18] K. Zhou, F. Shen, G. Yin, L. Zhang, Optical fiber micro-devices made with femtosecond laser, in: *Advanced Photonics 2016 (IPR, NOMA, Sensors, Networks, SPPCom, SOF)*, OSA, 2016. doi:10.1364/sensors.2016.sew3d.1.
- [19] C. J. Bellair, C. L. Curl, B. E. Allman, P. J. Harris, A. Roberts, L. M. Delbridge, K. A. Nugent, Quantitative phase amplitude microscopy IV: Imaging thick specimens, *Journal of Microscopy* 214 (1) (2004) 62–69. doi:10.1111/j.0022-2720.2004.01302.x.
- [20] J. Canning, Fibre gratings and devices for sensors and lasers, *Laser & Photonics Review* 2 (4) (2008) 275–289. doi:10.1002/lpor.200810010.

- [21] S. Zhang, W. Zhang, S. Gao, P. Geng, X. Xue, Fiber-optic bending vector sensor based on Mach-Zehnder interferometer exploiting lateral-offset and up-taper, *Optics Letters* 37 (21) (2012) 4480–4482. doi:10.1364/ol.37.004480.

445